Experimental Validation of CFD Simulations of a Lab-Scale Fluidized-Bed Reactor with and Without Side-Gas Injection

Jian Min
Dept. of Chemical and Biological Engineering, Iowa State University, Ames, IA 50010

Joshua B. Drake and Theodore J. Heindel
Dept. of Mechanical Engineering, Iowa State University, Ames, IA 50010

Rodney O. Fox
Dept. of Chemical and Biological Engineering, Iowa State University, Ames, IA 50010

DOI 10.1002/aic.12077
Published online October 23, 2009 in Wiley InterScience (www.interscience.wiley.com).

Fluidized-bed reactors are widely used in the biofuel industry for combustion, pyrolysis, and gasification processes. In this work, a lab-scale fluidized-bed reactor without and with side-gas injection and filled with 500–600 μm glass beads is simulated using the computational fluid dynamics (CFD) code Fluent 6.3, and the results are compared to experimental data obtained using pressure measurements and 3D X-ray computed tomography. An initial grid-dependence CFD study is carried out using 2D simulations, and it is shown that a 4-mm grid resolution is sufficient to capture the time- and spatial-averaged local gas holdup in the lab-scale reactor. Full 3D simulations are then compared with the experimental data on 2D vertical slices through the fluidized bed. Both the experiments and CFD simulations without side-gas injection show that in the cross section of the fluidized bed there are two large off-center symmetric regions in which the gas holdup is larger than in the center of the fluidized bed. The 3D simulations using the Syamlal-O'Brien and Gidaspow drag models predict well the local gas holdup variation throughout the entire fluidized bed when compared to the experimental data. In comparison, simulations with the Wen-Yu drag model generally over predict the local gas holdup. The agreement between experiments and simulations with side-gas injection is generally good, where the side-gas injection simulates the immediate volatilization of biomass. However, the effect of the side-gas injection extends further into the fluidized bed in the experiments as compared to the simulations. Overall the simulations under predict the gas dispersion rate above the side-gas injector. © 2009 American Institute of Chemical Engineers *AIChE J,* 56: 1434–1446, 2010
Keywords: biofuel processing, fluidized-bed reactor, gas holdup, multiphase flow, tomography

Correspondence concerning this article should be addressed to R. O. Fox at rofox@iastate.edu.

Introduction

Fluidized beds are commonly used by the chemical, mineral, pharmaceutical, and energy industries because of low

pressure drops, uniform temperature distributions, and high energy- and mass-transfer rates. In the biofuel industry, fluidized-bed reactors are central components for combustion, pyrolysis, and gasification processes. The local gas holdup (or solids voidage) distribution in the fluidized bed is an extremely important parameter in practical systems, determining the uniform mass and energy distributions and gasification efficiency. Because of the rapid time scales associated with the fluidization dynamics, time-averaged (as opposed to instantaneous) data are often more meaningful than transient data in the design of commercial-scale fluidized-bed reactors.

Because the bed material (solid phase) is typically opaque in gas–solid systems, it is difficult to obtain detailed local data (either instantaneous or time-averaged) for the entire bed. As fluidization is a dynamic process, invasive monitoring methods can influence the internal flow, thereby reducing the reliability of the measurements. Currently, noninvasive monitoring techniques are the methods-of-choice when investigating fluidized beds. The available techniques include electrical capacitance tomography, ultrasonic computed tomography, gamma densitometry tomography, X-ray fluoroscopy (radiography/stereography), and X-ray computed tomography (see Heindel et al.[1] for details). Franka et al.[2] used X-ray computed tomography (CT) and radiography to analyze differences in biofuel-related materials for fluidized beds operating under three different gas flow rates. The CT images showed that glass beads fluidized much more uniformly compared to melamine and ground corncob beds. However, crushed walnut shells fluidized more uniformly as the gas flow rate increased.

Design of commercial-scale fluidized-bed reactors traditionally depends on pilot-scale experiments, which are expensive, often difficult to setup, and time consuming. Thus, there has been an increasing use of computational fluid dynamics (CFD) to complement industrial design of fluidized-bed reactors. Nevertheless, the situation is complex whenever multiphase flows are involved because transport equations for mass, momentum, and turbulence properties have to be solved for each phase. A few researchers, summarized by Cui et al.,[3] have attempted to study biofuel-related process characteristics in fluidized-bed reactors using CFD and some progress has been made, focusing on terminal settling velocities, minimum fluidization and fluidizability, and the residence time of biomass particles. Most CFD simulations of fluidized beds in the literature are two-dimensional (2D), mostly due to a lack of the computer resources needed for grid-independent 3D simulations. Even with today's advanced computational facilities, 3D simulations are still expensive as the equations have to be integrated using small time steps over long periods to compute time averages of the inherently chaotic and transient fluidization process.

To save computing time, some past studies have compared 2D vs. 3D simulations. Peirano et al.[4] performed numerical simulations of a rectangular bubbling fluidized bed using ESTET/ASTRID. Numerical results were compared to experimental values for the power spectra of pressure fluctuations, bed height, and probability density function of particle volume fraction. Cammarate et al.[5] also validated the bubbling behavior predicted by 2D and 3D simulations of a rectangular fluidized bed using CFX4.4. Bed expansion, bubble holdup and bubble size calculated from 2D and 3D simulations were compared with predictions obtained from Darton et al.[6] In almost all cases, a more realistic physical behavior of fluidization was obtained using 3D simulations. Both Peirano et al.[4] and Cammarate et al.[5] concluded that 3D simulations are preferred, except maybe in cases where the flow is by nature two-dimensional. Xie et al.[7] investigated bubbling, slugging and turbulent regimes in 2D and 3D simulations for both cylindrical and rectangular domains using the numerical code Multiphase Flow with Interphase eXchanges (MFIX). The results demonstrated that a 2D Cartesian grid could be used to successfully simulate and predict a bubbling regime. However, caution must be exercised when using 2D Cartesian coordinates for other fluidized regimes. Papadikis et al.[8] calculated the forces exerted on the particles in fluidized beds as well as the velocity components in 2D and 3D simulations using Fluent 6.2. It was shown that the hydrodynamics of the bed changed significantly from the 2D to 3D simulations. The bubbles in 3D were formed close to the gas inlet of the reactor compared with the 2D case. The 3D simulations were also more accurate with respect to heat, mass and momentum transport. Moreover, in many biofuel processing applications, the fluidized-bed reactors have side-gas injection in order to feed the biomass into the reactor, for which 3D simulations are required. It is thus important to understand how well the full 3D CFD simulations predict the fluid dynamics of fluidized-bed reactors with geometry and operating conditions representative of biofuel processing (e.g., polydisperse solids with different sizes and densities).

The long-term goal of our research is to find a systematic method for the design of commercial-scale fluidized-bed reactors using CFD simulations validated using lab-scale experimental techniques. The use of X-ray computed tomography to quantitatively obtain the local time-averaged gas holdup in the lab-scale fluidized-bed reactors is a key component. In this work, experimental validation of local gas-holdup predictions from grid-independent CFD simulations using Fluent 6.3 are reported for a bubbling fluidized bed with and without side-gas injection. Both quantitative and qualitative local gas holdup distributions calculated using 3D X-ray flow visualization measurements are compared to the CFD predictions. Simulation results using three different drag models (Syamlal-O'Brien, Gidaspow, Wen-Yu) are compared in order to determine which model is best suited for fluidized-bed simulations. The overall study is useful in understanding how gas holdup is distributed throughout a fluidized bed under different operating conditions (e.g., with and without side-gas injection). Furthermore, the study establishes the minimal requirements (e.g., grid resolution, drag model, model parameters) for setting up CFD simulations that could be used to design commercial-scale fluidized-bed reactors for biofuel processing.

Experimental Setup

Fluidized-bed reactor

The lab-scale fluidized-bed reactor, shown in Figure 1, was fabricated from three 152 mm ID acrylic tube sections with 12.7-mm-thick acrylic flange plates attached to each end. The three sections measure 150 mm, 300 mm, and

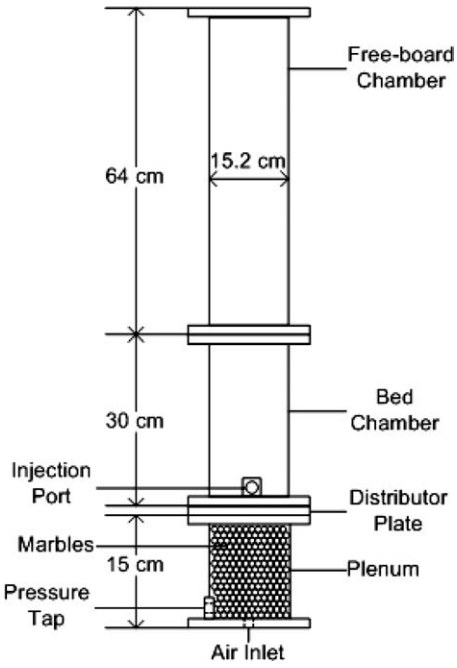

Figure 1. Schematic of the lab-scale fluidized-bed reactor.

640 mm in length, respectively, for the plenum, reactor, and freeboard chambers. Between the plenum and bed chamber is a 1.2-mm-thick stainless steel perforated aeration plate containing one hundred and thirty 1-mm-diameter holes that are approximately equally spaced in concentric rings to ensure homogeneous gas distribution and a low pressure drop. The aeration plate has an open area ratio of 0.57%. Air is introduced into the system by a single inlet in the bottom of the plenum. The air travels through the marble-filled plenum and is dispersed evenly over the bottom of the aeration plate. Rubber gaskets are placed between each flange, sealing the various components and forcing all gas to flow directly through the bed and out the top. A pressure tap in the bottom of the plenum holds a transducer connected to a data acquisition card to record inlet pressure. A second tap on the side of the fluidized bed 25 mm above the aeration plate is used for side-gas injection. Compressed air was used as the operating gas in all experiments.

The bed material was composed of 500–600-μm-diameter glass beads, Geldart Group B, due to their excellent fluidization properties. The key features of these particles are rapid deaeration when the gas is shut off, large bubbles, and intermediate solids mixing. Gas and solid properties of the fluidized bed used in the experiments and CFD simulations are listed on Table 1.

Pressure drop and minimum fluidization velocity

The minimum fluidization velocity, U_{mf}, is one of the most important fundamental parameters in fluidization. U_{mf} is a complex function of particle properties/geometry, fluid properties, and bed geometry, and may be calculated from literature correlations.[9,10] Typically, the correlations predict U_{mf} within $\sim\pm25\%$, and it is generally best to measure U_{mf} experimentally whenever possible[11]; this is the approach adopted in this work.

Table 1. Bed Material Properties

Properties	Units	Values
Solid–glass beads		
Particle Diameter	μm	500–600
Particle Density	kg/m^3	2600
Particle Sphericity	–	1
Coefficient of Restitution	–	0.9
Static Bed Height	mm	152
Angle of internal friction	–	30°
Packing Limit	–	0.63
Friction Packing Limit	–	0.61
Initial Solid Volume Fraction	–	0.575
Gas–pressured air		
Density	kg/m^3	2.417
Viscosity	N s/m^2	1.8×10^{-5}

The onset of fluidization occurs when the drag force by upward moving gas equals the weight of the particles. Hence, U_{mf} is defined as the point where the pressure drop across the bed stops increasing linearly with gas velocity and remains constant. In a bed at the onset of fluidization, the voidage is somewhat larger than in a packed bed, and actually corresponds to the loosest state of packing. Figure 2 gives detailed data of pressure drop vs. superficial gas velocity for nine experimental data sets for our fluidized-bed reactor. For our reactor, U_{mf} is equal to 0.195 m/s with no side-gas injection. In this work, all results (experimental and computational) are obtained with the fluidized bed operating at $U_g = 2U_{mf} = 0.39$ m/s.

X-ray system

Iowa State University's XFloViz facility, shown in Figure 3, is used in this work to image the fluidized bed and has been described in detail elsewhere.[1,12] Thus, only a brief overview will be presented here. Two LORAD LPX200 portable X-ray tubes provide the X-rays. Current and voltage can be adjusted from 0.1 to 10.0 mA and 10 to 200 kV,

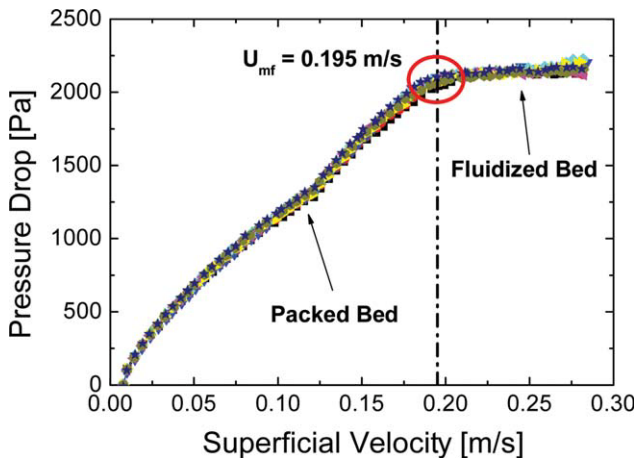

Figure 2. Experimental pressure drop reading for a bubbling fluidized bed.

[Color figure can be viewed in the online issue, which is available at www.interscience.wiley.com.]

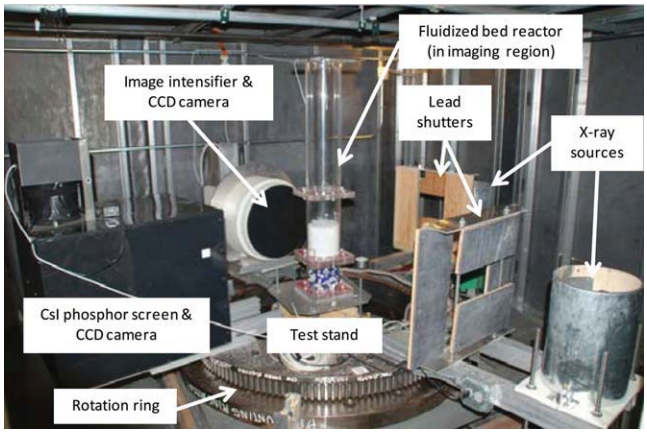

Figure 3. X-ray imaging facility.

[Color figure can be viewed in the online issue, which is available at www.interscience.wiley.com.]

respectively, with a maximum power of 900 W. Low energy radiation is suppressed by two 1-mm-thick copper filters and one aluminum filter placed directly in front of the X-ray sources.

Located opposite each X-ray source is an X-ray detector/CCD camera pair. The CsI phosphor screen and CCD camera in Figure 3 was used to acquire the CT data because of its high spatial resolution. This camera is located opposite one of the sources, shown in Figure 3, and is connected to a square 440 × 440 mm cesium-iodide (CsI) scintillator screen, which transforms radiation into visible light. A 50 mm Nikon lens captures images, which are digitized by an Apogee Alta U9 system. This system has 3072 × 2048 pixels and is thermoelectrically cooled to allow long exposure times. Usually, an exposure time of one second with 4 × 4 binning is chosen to minimize acquisition time while maintaining the signal strength. The detector system and source pair are located on a 1.0 m ID rotation ring that can rotate 360° around the fluidized bed.

Data from the CCD cameras are acquired by software developed by Iowa State University's Center for Nondestructive Evaluation (CNDE) and a personal computer with 4 GB of RAM. The software allows for camera control, as well as motion control for the rotation ring. Images acquired by the CCD camera with the CsI screen are normalized for pixel nonuniformity (linearization) and corrected for beam hardening. These corrections are performed using custom algorithms. Volumetric reconstruction of the CT images is performed using CNDE's 64-node LINUX cluster using a filtered back projection algorithm. Additional details of the X-ray imaging system are provided by Heindel at al.[1]

Gas holdup analysis method

Gas holdup is calculated using three different CTs: the dynamic fluidized bed operating under the desired conditions, a static bed, and an empty bed. Theoretically, local gas holdup (ε_g) is determined by knowing the local X-ray attenuation for the dynamic fluidized bed (A), an individual particle (A_p), and the gas (A_g). As attenuation is proportional to CT intensity, the local gas holdup can be calculated at each individual CT voxel (3D pixel) position. Each dynamic fluidized bed CT (I), particle (I_p), and gas (I_g) voxel is assigned a value representing the local intensity at that position. Hence, ε_g is determined by

$$\varepsilon_g = \frac{A - A_p}{A_g - A_p} = \frac{I - I_p}{I_g - I_p} \tag{1}$$

The CT intensity for a single particle cannot be determined due to the small size of each particle. However, by manipulating the bulk-phase gas holdup equation, the CT intensity for a static (bulk) bed of particles (I_b) can be substituted instead. In this case, the void fraction for the bulk material ($\varepsilon_{g,b}$) can be calculated from CT intensities of the static (bulk) bed:

$$\varepsilon_{gb} = \frac{I_b - I_p}{I_g - I_p} \tag{2}$$

For a homogenous granular material, the void fraction of the bulk material is assumed constant, and is defined by

$$\varepsilon_{gb} = 1 - \frac{\rho_b}{\rho_p} \tag{3}$$

where ρ_b is the bulk density (experimentally determined) and ρ_p is the particle density for the bed material (provided by the supplier). Substituting and rearranging Eq. 1 and 2 yields the local gas holdup:

$$\varepsilon_g = \frac{I - I_b + (I_g - I)\varepsilon_{gb}}{I_g - I_b} \tag{4}$$

In the configuration for this study, the CT images have a voxel size of $\sim 0.6 \times 0.6 \times 0.6$ mm^3. Because of the time-averaged data, the spatial resolution in the dynamic region of the fluidized bed is difficult to quantify, but for static objects, we have been able to resolve objects on the order of 2 mm. Because of the nature of X-rays, it is expected that a comparable resolution will be obtained in the time-averaged images of the dynamic region. Estimated absolute uncertainty in the local gas holdup values is ± 0.04. This is a worst-case estimate where most of the data fall within an absolute gas holdup value of ± 0.02.

CFD modeling

CFD simulations of the lab-scale fluidized-bed reactor are carried out with Fluent 6.3 on the High Performance Computing (HPC) machines at Iowa State University. CFD uses numerical methods to solve partial differential equations that model the fluid dynamics. In general, CFD can be applied to reactive, multiphase, laminar, and turbulent flows. In this work, governing equations for mass, momentum, and energy for each phase (gas and solid) are solved within a geometrical domain that corresponds to the lab-scale fluidized-bed reactor used in the experiments.

Computational grid

A Cartesian coordinate system is used for grid generation, where hexahedral elements are formed for the 3D geometry

Table 2. Grid Sizes for the 2D and 3D Simulations

Dimensions	Name	X (mm)	Y (mm)	Z (mm)	Cell Number	Node Number
2D	2D-8	8	8	–	$19 \times 38 = 722$	780
	2D-4	4	4	–	2888	3003
	2D-2	2	2	–	11,552	11,781
	2D-1	1	1	–	46,208	46,665
3D	3D-bottom	4	4	4–6	59,400	62,883
	3D-side	4.38	4.38	5.42	59,400	62,883
	3D-4	4	4	4–6	59,400	62,883

and quadrilateral elements for the 2D geometry. Grid generation specifics are shown in Table 2. Note that for the 2D simulations we carried out a grid-refinement study by varying the grid size by factors of two for four different grids: 8×8 mm^2, 4×4 mm^2, 2×2 mm^2, and 1×1 mm^2, respectively. For the grid-refinement study, a square mesh was used because uniform and regularly structured grids provide quick convergence with minimal numerical errors. The grid sizes shown for the 3D cases are approximate (since the grid cells are not square) and equal to sample values at the height of the side injection. A sample 2D grid and 3D grid with side-gas injection are shown in Figure 4. In the 2D grid, X is the radial coordinate and Y is the axial coordinate. In the 3D grid, the X and Y directions are along the horizontal cross section of the reactor and the Z direction is along the height of the reactor. In the Z direction, the grid size varied from 4 mm at the bottom to 6 mm at the top. The center of the base of the reactor is considered the origin and the reactor walls are located 76 mm from the origin with a height of 304 mm. For the 3D grid, $Y = 0$ and $X = 0$ represents a plane cut through the origin and corresponds to experimental X-Z and Y-Z slices of a CT image. This information is useful in understanding the results, which can be compared with the experimental data qualitatively and quantitatively.

When side-gas injection is simulated, the injection-port diameter is set to 11 mm with an open area of 95 mm^2. The distance between the center of the side-gas injection port and the aeration plate is 30 mm. To obtain better meshes, the cross section of the side-gas injector is represented by a rectangle. The same 3D mesh is used in cases with and without side-gas injection. The location of the side-gas injection is shown in Figure 4b by the four gray-sided rectangles. Also, because of meshing constraints, it was difficult to model exactly the aeration plate containing one hundred and thirty 1-mm-diameter holes used in the experiments. Hence, a uniform inlet gas velocity distribution was used in all simulations.

Multiphase model

There are two approaches for CFD modeling of gas–solid flows: the Euler-Lagrange model[13–18] and the Euler-Euler model.[5,7,8,16,17,19–24] Using the Euler-Lagrange model, trajectories of individual particles are tracked by solving the equations of motion, whereas the gas phase is modeled using an Eulerian framework. As a consequence, the Euler-Lagrange model requires large computational resources for large systems of particles (such as the one used in our experiments). With the Euler-Euler model, the base assumption is that the gas and solid phases are interpenetrating continua. Therefore, the Euler-Euler model derived from the kinetic theory of granular flows (KTGF)[25] is the more commonly used CFD model to predict the dynamic behavior of dense fluidized-bed reactors.

In the Euler-Euler approach, the different phases are treated mathematically as interpenetrating continua. As the volume of a phase cannot be occupied by the other phases, the concept of phase volume fraction is introduced. These volume fractions are assumed to be continuous functions of space and time and their sum is equal to one. Conservation equations for mass and momentum for each phase are derived using the KTGF for inelastic spherical particles to obtain a set of partial differential equations. The relevant equations in Fluent 6.3 for the Euler-Euler model for dense gas-particle flows are listed in Table 3.

Consistent with the experiments, in our simulations mass transfer between the phases and external body (except gravity) forces are set to zero. Likewise, due to the density difference between the solid particles and the gas phase, lift and virtual mass forces are assumed to be negligible in the momentum equations. For granular flows in the compressible regime (i.e., where the solids volume fraction is less than its maximum allowed value), a solids pressure (different from the fluid-phase) is calculated independently and used for the pressure gradient term, ∇p_s, in the granular-phase momentum equation. The solids pressure due to particle collisions is calculated using the equation from Lun et al.[26] The radial distribution function of Lun et al.[26] takes into account the probability of particles colliding with each other when the granular phase becomes densely packed.

In our simulations, the transfer of forces between the fluid and solid phases is described by one of the empirical drag

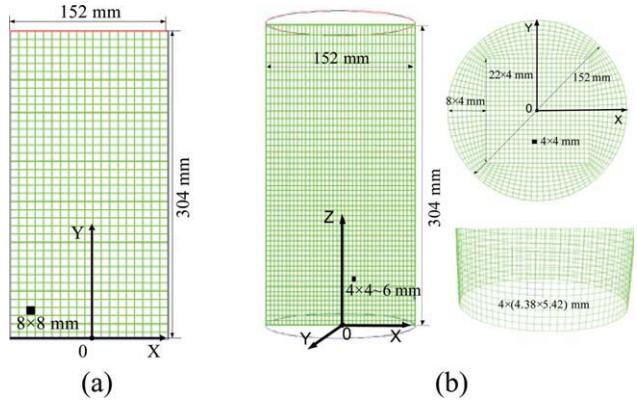

Figure 4. Schematic of grid. (a) 2D-8. (b) 3D with side-gas injection.

[Color figure can be viewed in the online issue, which is available at www.interscience.wiley.com.]

Table 3. Model Equations for the Euler-Euler Model in Fluent 6.3

Contents	Equation
Gas-phase continuity	$\frac{\partial}{\partial t}(\varepsilon_g \rho_g) + \nabla \cdot (\varepsilon_g \rho_g v_g) = 0$
Solid-phase continuity	$\frac{\partial}{\partial t}(\varepsilon_s \rho_s) + \nabla \cdot (\varepsilon_s \rho_s v_s) = 0$
Gas-phase momentum	$\frac{\partial}{\partial t}(\varepsilon_g \rho_g v_g) + \nabla(\varepsilon_g \rho_g v_g v_g) = -\varepsilon_g \nabla p_g + \nabla \cdot \bar{\bar{\tau}}_g + \varepsilon_g \rho_p g + K_{sg}(v_s - v_g)$
Solid-phase momentum	$\frac{\partial}{\partial t}(\varepsilon_s \rho_s v_s) + \nabla(\varepsilon_s \rho_s v_s v_s) = -\varepsilon_s \nabla p_g - \nabla p_s + \nabla \cdot \bar{\bar{\tau}}_s + \varepsilon_s \rho_s g + K_{gs}(v_g - v_s)$
Solid pressure (Lun et al.)	$p_s = \varepsilon_s \rho_s \theta_s + 2\rho_s (1 + e_{ss}) \varepsilon_s^2 \theta_s g_{0,ss}$
Radial distribution function (Lun et al.)	$g_{0,ss} = \left[1 - \left(\frac{\varepsilon_s}{\varepsilon_{s,max}}\right)^{1/3}\right]^{-1}$
Viscous stress tensor	$\bar{\bar{\tau}}_p = \varepsilon_p \mu_p \left(\nabla v_p + \nabla v_p^T\right) + \varepsilon_p \left(\lambda_p - \frac{2}{3}\mu_p\right) \nabla \cdot v_p \bar{\bar{I}}, p = g, s$
Solid-phase Reynolds number	$Re_s = \frac{\rho_g d_s \lvert v_s - v_g \rvert}{\mu_g}$
Syamlal-O'Brien drag model	$K_{sg} = \frac{3\varepsilon_s \varepsilon_g \rho_g}{4 v_{r,s}^2 d_s} \left(0.63 + \frac{4.8}{\sqrt{Re_s / v_{r,s}}}\right)^2 \left(\frac{Re_s}{v_{r,s}}\right) \lvert v_s - v_g \rvert$ $v_{r,s} = 0.5\left(\varepsilon_g^{4.14} - 0.06 Re_s + \sqrt{(0.06 Re_s)^2 + 0.12 Re_s (2B - \varepsilon_g^{4.14}) + \varepsilon_g^{8.28}}\right)$ $\varepsilon_g \le 0.85, B = 0.8 \varepsilon_g^{1.28}$ $\varepsilon_g > 0.85, B = \varepsilon_g^{2.65}$
Gidaspow drag model	$K_{sg} = 150 \frac{\varepsilon_s (1 - \varepsilon_g) \mu_g}{\varepsilon_g d_s^2} + 1.75 \frac{\rho_g \varepsilon_s}{d_s} \lvert v_s - v_g \rvert, \varepsilon_g \le 0.8$ $K_{sg} = \frac{3\varepsilon_s \varepsilon_g \rho_g}{4 d_s} \left(\frac{24}{\varepsilon_g Re_s}\left[1 + 0.15(\varepsilon_g Re_s)^{0.687}\right]\right) \varepsilon_g^{-2.65} \lvert v_s - v_g \rvert, \varepsilon_g > 0.8$
Wen-Yu drag model	$K_{sg} = \frac{3\varepsilon_s \varepsilon_g \rho_g}{4 d_s} \left(\frac{24}{\varepsilon_g Re_s}\left[1 + 0.15(\varepsilon_g Re_s)^{0.687}\right]\right) \varepsilon_g^{-2.65} \lvert v_s - v_g \rvert$
Solid shear viscosity	$\mu_s = \mu_{s,col} + \mu_{s,kin} + \mu_{s,fr}$
Collisional viscosity	$\mu_{s,col} = \frac{4}{5} \varepsilon_s \rho_s d_s g_{0,ss} (1 + e_{ss}) \left(\frac{\theta_s}{\pi}\right)^{\frac{1}{2}}$
Kinetic viscosity (Syamlal et al.)	$\mu_{s,kin} = \frac{\varepsilon_s d_s \rho_s \sqrt{\theta_s \pi}}{6(3 - e_{ss})}\left[1 + \frac{2}{5}(1 + e_{ss})(3e_{ss} - 1)\varepsilon_s g_{0,ss}\right]$
Frictional viscosity (Shaeffer)	$\mu_{s,fr} = \frac{p_s \sin\phi}{\sqrt{I_{2D}}}$
Solid bulk viscosity (Lun et al.)	$\lambda_s = \frac{4}{3} \varepsilon_s \rho_s d_s g_{0,ss} (1 + e_{ss}) \left(\frac{\theta_s}{\pi}\right)^{\frac{1}{2}}$
Granular temperature	$\frac{3}{2}\left[\frac{\partial}{\partial t}(\rho_s \varepsilon_s \theta_s) + \nabla \cdot (\rho_s \varepsilon_s v_s \theta_s)\right] = \left(-p_s \bar{\bar{I}} + \bar{\bar{\tau}}_s\right) : \nabla v_s + \nabla \cdot (k_{\theta_s} \nabla \theta_s) - \gamma_{\theta_s} + \Phi_{gs}$ $\gamma_{\theta s} = \frac{12(1 - e_{ss}^2) g_{0,ss}}{d_s \sqrt{\pi}} \rho_s \alpha_s^2 \theta_s^{3/2}, \phi_{gs} = -3 K_{gs} \theta_s$

laws proposed by Syamlal,[27] Gidaspow,[21] and Wen and Yu.[10] The solids stress tensor contains shear and bulk viscosities arising from particle momentum exchange due to translation and collision. A frictional component of the viscosity can also be included to account for the viscous-plastic transition that occurs when particles of a solid phase reach the maximum solids volume fraction. The collisional and kinetic parts, and the optional frictional part, are added to give the solids shear viscosity. The collisional viscosity is calculated using the equation from Gidaspow.[21] It is assumed that the angle of internal friction does not influence the results significantly since, for a gas–solid system, van Wachem et al.[17] concluded that the choice of solid stress models or radial distribution functions do not have a significant impact on the results. The kinetic part of the granular viscosity and the granular conductivity are both obtained from relationships proposed by Syamlal et al.[28] The expression of Schaeffer[29] is used for frictional viscosity, with an angle of internal friction of 30°. The solids bulk viscosity accounts for the resistance of the granular particles to compression and expansion and has the form proposed by Lun et al.[26] The frictional stress is added to the stress predicted by the kinetic theory when the solids volume fraction is high. In this work the frictional stress is based on the KTGF.

The granular temperature for the solids phase is proportional to the kinetic energy of the random motion of the

Table 4. Simulation Model Parameters in Fluent 6.3

Description	Value	Comment
Pressure-based solver	2ddp, 3ddp	Double-Precision
Unsteady formulation		Second order implicit
Time steps	10^{-4} to 10^{-3} s	Specified
Maximum number of iterations	50	Specified
Data sampling for time statistics	10	Sampling interval
Operating pressure	1 atm	Specified
Operating density	2.417 kg/m^3	Gas-phase density
Gravitational acceleration	9.81 m/s^2	Gravitation
Inlet boundary conditions	0.39 m/s	Superficial gas velocity
Inlet of side-gas injection	7.446 m/s	Normal to boundary
Outlet boundary conditions	Outflow	Fully developed flow
Wall boundary for gas-phase	No slip	Specified momentum
Wall boundary for solid-phase	0 Pa	Specified shear stress
Convergence criteria	10^{-4}	Specified
Pressure-velocity coupling	SIMPLE	Phase-coupled
Momentum discretization	Second-order upwind	
Volume fraction discretization	QUICK	

particles. Here the algebraic formulation is used, in which the convection and diffusive terms of the transport equation derived from KTGF[28] are neglected. Note that the use of a single particle temperature (as opposed to a full second-order model such as the one proposed by Simonin[23]) will be valid for highly collisional granular flows where the particle velocity distribution remains close to the Maxwellian form. Because of the relatively high solids volume fraction in our fluidized-bed reactor, the solids phase should be highly collisional.

Numerical methodology

The time step for the simulations is calculated based on the convective Courant-Friedrichs-Levy (CFL) condition, which depends on the ratio of the grid size and maximum velocity in the flow domain. For the results reported below, the time step is set in the range of 10^{-3} to 10^{-4} s, depending on simulation conditions. The numerical convergence criterion (as defined in Fluent 6.3) is set to 10^{-4}. Second-order discretization schemes are used for the spatial and temporal derivatives. Simulations were performed from $t = 0$ to 70 s. Statistics are not saved from the calculations for $t < 10$ s to make sure the initial transients die down. Since the experimental data are time-averaged, all comparisons will be based on time-averaged simulation results that span 10–70 s. The simulation model parameters are listed in Table 4. To determine the sensitivity of the simulation results to the various model parameters, a large series of simulations were run for the (Geldart B) particle characteristic used in the experiments. In general, it was found that the quantities that could be measured experimentally (and hence were available for model validation) were insensitive to most model parameters, except the form of the drag model. Thus, we report only the results from the drag model study below.

Results and Discussion

Grid-independence study

An initial simulation study using 2D grids with increasing resolution was carried out in order to determine the grid size required for grid-independent simulations for our fluidized bed composed of Geldart B particles. The four different grids described in Table 2 (2D-8, 2D-4, 2D-2, and 2D-1) were used to discretize the 2D flow domain into square cells and then the results were compared. In the bubbling bed region, experimental measurements (i.e., Figure 2) reveal a constant bed pressure drop of ~2160 Pa. All 2D and 3D simulations at $U_g = 2U_{mf}$ predict a bed pressure drop between 2140 Pa and 2180 Pa. These results show that the predicted and experimental pressure drop for a bubbling fluidized bed are approximately equal. Moreover, as discussed below, the bed height, which is known[30] to be very sensitive to the grid resolution and to 2D vs. 3D simulations, is in good agreement with the experimental measurements. These observations provide confidence that the gross bed behavior is modeled correctly.

Figure 5 shows contour plots of the time-averaged gas holdup in a 2D fluidized bed operating at $U_g = 2U_{mf}$. The gas velocity distribution at the gas inlet was uniform for all grids. The overall bulk time-averaged gas holdup

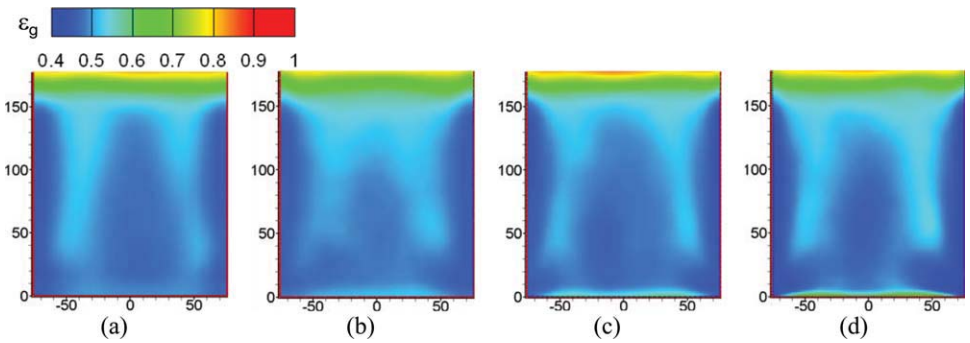

Figure 5. Time-averaged gas holdup in a glass bead fluidized bed in simulations.

(a) 2D-8. (b) 2D-4. (c) 2D-2. (d) 2D-1. [Color figure can be viewed in the online issue, which is available at www.interscience.wiley.com.]

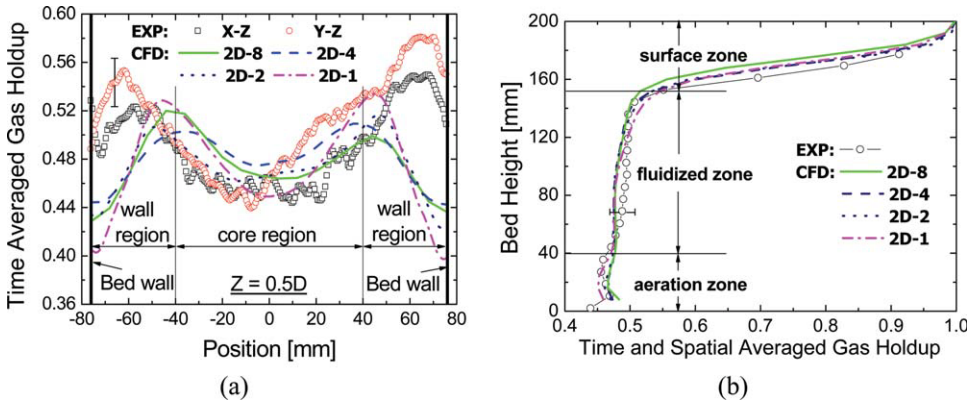

Figure 6. Local gas holdup in 2D simulations and 3D experiments.

(a) Time-averaged values at horizontal level $Z = 0.5D$. (b) Time- and spatial-averaged values along the height of bed. The error bar in each figure is typical of all experimental data. [Color figure can be viewed in the online issue, which is available at www.interscience.wiley.com.]

distributions showed no substantial changes among the different 2D grids. Quantitative time-averaged local gas holdup predictions using the four different grids are compared to the experimental results in Figure 6. Figure 6a is the time-averaged gas holdup at a horizontal level of $Z = 0.5D$, where the horizontal positions at ± 76 mm correspond to the bed walls. There are two regions in the cylindrical geometry, divided by ± 38 mm: the core region and wall regions. The errorbar in Figure 6a represents an absolute gas holdup error of ± 0.02, which is typical of most data. The error bar is provided only for one data point to avoid confusion in the plot, but the error magnitude should be applied to all experimental data.

For comparison, experimental values for the 3D fluidized bed were obtained along mutually perpendicular rays at specified Z heights (i.e., from the X-Z and Y-Z CT slices). The local fluctuations in the experimental data are due, primarily, to experimental noise. Additionally, the narrow gas holdup range for the vertical axis accentuates the local fluctuations. In comparison to the experimental data, for all grids the gas holdup is generally over predicted slightly in the core region, but under predicted in the wall region. The results do not improve by further decreasing the grid size (perhaps due to the 2D vs. 3D representation used in the simulations).

Figure 6b is the time-averaged and horizontal-slice-averaged gas holdup along the height of the fluidized bed for the CFD simulations. The experimental data come from CT slice-averaged data at the given height. Again, the error bar represents typical experimental error ranges associated with the experimental data. Three zones are identified: the aeration zone ($Z = 0$–38 mm), the fluidized zone ($Z = 38$–152 mm), and the surface zone in the upper portion of the bed. The experimental gas holdup just above the distributor is smaller due to the effect of the plate, where gas jetting is observed and not all holes are active. Because of the uniform inlet profile used in the CFD simulations, no jetting phenomena are predicted with CFD.

In general, the 2D-1 grid gives the best overall agreement with the experimental data, while the 2D-4 and 2D-2 grids give better results in the upper portion of the bed. Based on a detailed analysis of the local time-averaged and time- and spatial-averaged gas holdup throughout the fluidized bed, it is concluded that the 4-mm grid provides a good compromise between computational accuracy and expense and is sufficient for simulating the fluidized-bed reactor used in our work. This conclusion is consistent with the findings of Parmentier et al.[30] who showed that fluidized-bed simulations are relatively insensitive to grid resolution for Geldart B particles. Hence, an $\sim$4-mm grid is recommended for 3D simulations of the plant-scale fluidized-bed reactor for the operating conditions used in this work. Note, however, that the required grid resolution will depend on the physics of the problem and, for example, a finer grid would be required for Geldart Group A/B or A particles in order to predict the correct bed height.[30,31]

Drag model study

Using the $\sim$4-mm grid (Table 2), 3D simulations using the drag models of Syamlal-O'Brien, Gidaspow, and Wen-Yu were compared in detail with the experimental data. Figure 7 shows selected contour plots of the time-averaged gas holdup in the fluidized bed operating at $U_g = 2U_{mf}$, comparing CFD results using different drag models with the experiment data at mutually perpendicular X-Z and Y-Z slices. Comparing the experimental CT images in Figure 7, the X-Z and Y-Z slices show local variations near the aeration plate, particularly the presence of jetting near active aeration holes. The holes are oriented in a ring shape centered on the aeration plate, making it difficult to experimentally obtain axisymmetric inlet conditions in the X-Z and Y-Z slices. This is because CT images are reconstructed using a rectangular Cartesian coordinate system. Therefore, data can only be extracted on cross sections through the center of the reactor when $\theta = 0^\circ$ and 90° unless extensive data analysis is completed. Gas holdup in the Y-Z slice is larger in the right-hand side of the image than other regions of the bed, yet is approximately uniform throughout in the X-Z slice. This may result from the side-gas injection port modifying the local experimental boundary condition on the bed wall. Although the side-gas injector port is sealed, there are some

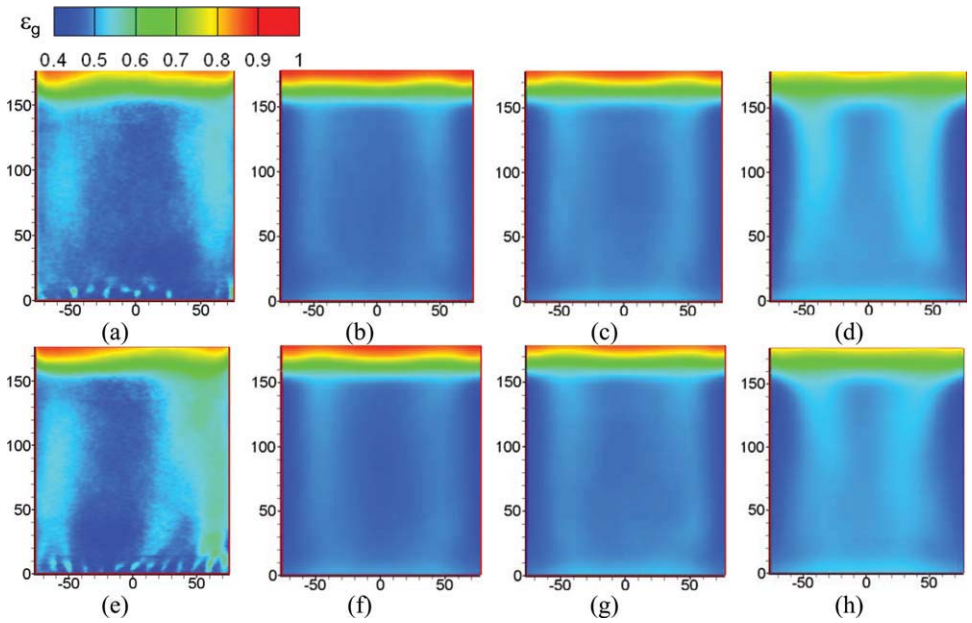

Figure 7. Time-averaged local gas holdup values.

(a) EXP X-Z. (b) Syamlal-O'Brien X-Z. (c) Gidaspow X-Z. (d) Wen-Yu X-Z. (e) EXP. Y-Z. (f) Syamlal-O'Brien Y-Z. (g) Gidaspow Y-Z. (h) Wen-Yu Y-Z. [Color figure can be viewed in the online issue, which is available at www.interscience.wiley.com.]

pressure differences causing the gas to circulate somewhat in the vicinity of the injector hole.

In the cross section of the fluidized bed, there are two large solids circulation zones in both the experiments and simulations, as shown in Figure 7. These are almost symmetric in the CFD simulations. The solids are forced by the gas phase to move upwards and concentrate in the middle of the fluidized bed, where there is a relatively small quantity of gas. Therefore, the gas holdup is smaller in the core region. After the gas carries the solids to the top of fluidized bed, it jets out and the solids are then circulated back down along the walls. Some bubbling gas is formed in the two circulation zones. Therefore, gas holdup is larger near the edge of the wall region (±38 mm) where the results found with the Wen-Yu drag model are qualitatively larger than the results from the Syamlal-O'Brien and Gidaspow drag models. The abrupt change in gas holdup near the top of the bed in the Wen-Yu simulations is higher than in the experiments and the other CFD simulations.

Quantitative local gas holdup comparisons between CFD simulations with the three drag models and experimental data are shown in Figure 8. The simulations under predict the experimental data in the wall region using the Syamlal-O'Brien drag model, as shown in Figure 8a. The simulations with the Gidaspow drag model also give good predictions in the core region compared with experimental data. The simulations with the Wen-Yu drag model predict much larger values in the core region without improving the predictions in the wall region. The value of time-averaged gas holdup in the core region is in the range 0.44–0.46, 0.46–0.48, and 0.49–0.51, respectively, for three drag models, compared with the experimental value of 0.44–0.53. The value in the

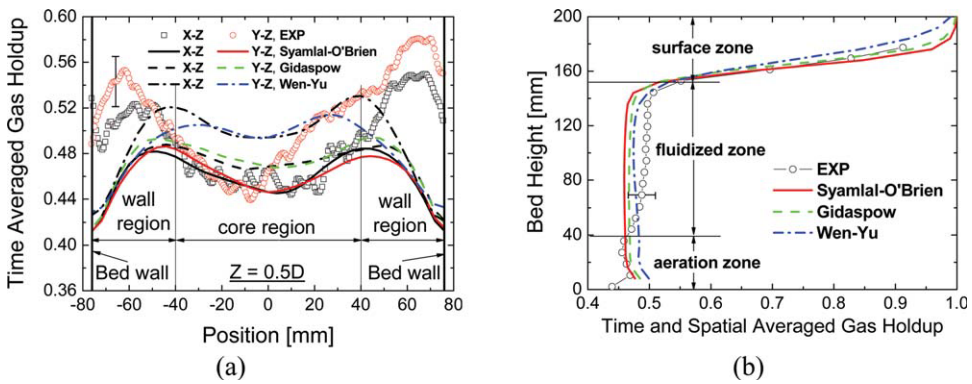

Figure 8. Local gas holdup in 3D simulations with different drag models compared to the experiments.

(a) Time-averaged values at horizontal level $Z = 0.5D$. (b) Time-averaged and spatial-averaged values along the height of bed. The error bar in each figure is typical of all experimental data. [Color figure can be viewed in the online issue, which is available at www.interscience.wiley.com.]

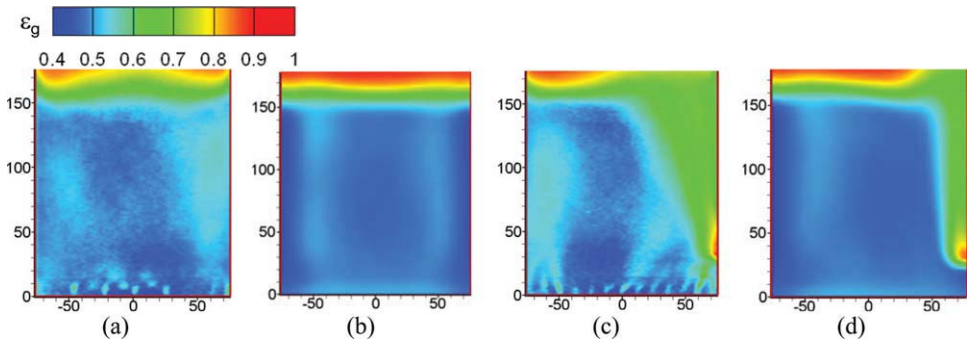

Figure 9. Time-averaged local gas holdup values in a glass bead fluidized bed with side-gas injection operating at $U_g = 2U_{mf}$ with $Q_s = 0.2Q_{mf}$.

(a) EXP X-Z. (b) CFD X-Z. (c) EXP Y-Z. (d) CFD Y-Z. [Color figure can be viewed in the online issue, which is available at www.interscience.wiley.com.]

wall region is in the range 0.41–0.48, 0.41–0.49, and 0.43–0.52, respectively, for the three drag models, and 0.48–0.58 in the experiments. The differences between the three CFD simulations are caused by the drag force. The results of the fluid-solid exchange coefficient K_{sg} are about 8200, 8900, and 11,000 in the fluidized region ($\varepsilon_g \sim 0.5$) for the Syamlal-O'Brien, Gidaspow, and Wen-Yu drag models, respectively. So the choice of drag models has a profound influence on the CFD simulation results of the fluidized beds.

Figure 8b gives the time- and spatial-averaged gas holdup values along the bed height. The predicted gas holdup results from the Syamlal-O'Brien (~0.46) and Gidaspow (~0.47) drag models are closer to the experimental measurements (~0.46) than those of the Wen-Yu drag model (~0.48) in the aeration zone. In comparison, in the fluidized zone the value is about 0.46, 0.47, and 0.47, respectively, for the three drag models, and about 0.50 for the experiments. Although the Wen-Yu drag model largely over predicts the gas holdup in the core region and under predicts it in the wall region (Figure 8a), this model shows better averaged predictions in the fluidized zone. Simulations with the Syamlal-O'Brien and Gidaspow drag models better predict the gas holdup variation throughout the bed height and in the transition region from the bulk bed to the freeboard. The height of the fluidized bed is over predicted by the Wen-Yu drag model, which is appropriate for dilute systems ($\varepsilon_g > 0.8$). Overall, the simulations with

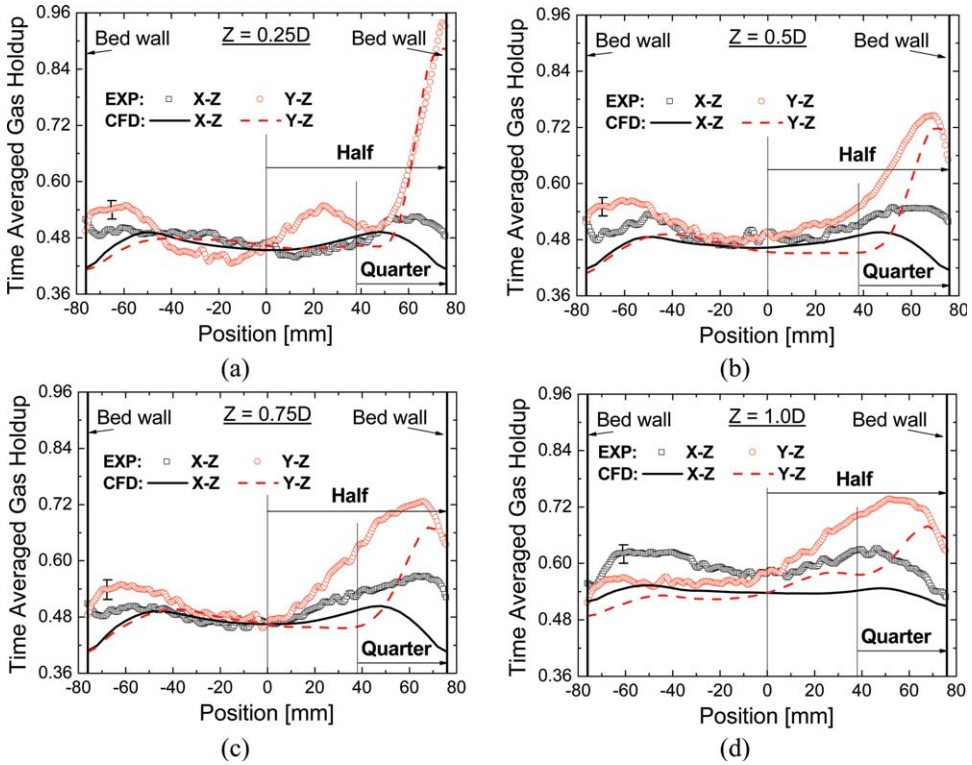

Figure 10. Time-averaged local gas holdup values operating at $U_g = 2U_{mf}$ with $Q_s = 0.2Q_{mf}$.

(a) $Z = 0.25D$. (b) $Z = 0.5D$. (c) $Z = 0.75D$. (d) $Z = 1.0D$. The error bar in each figure is typical of all experimental data. [Color figure can be viewed in the online issue, which is available at www.interscience.wiley.com.]

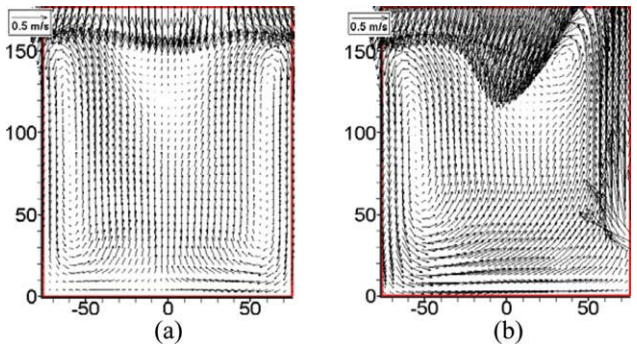

Figure 11. Time-averaged velocity field in a glass bead bed from 3D simulations in a Y-Z slice (a) without side-gas injection and (b) with side-gas injection.

[Color figure can be viewed in the online issue, which is available at www.interscience.wiley.com.]

the Syamlal-O'Brien and Gidaspow drag models yield better gas holdup predictions of the local gas holdup distribution throughout the fluidized bed.

Side-gas injection

The 3D CFD simulations were used to predict the gas holdup in the fluidized bed with side-gas injection that simulates the immediate volatilization of biomass. In all cases, the side-gas volumetric flow rate Q_s was set equal to $0.2Q_{mf}$ = 730 cm^3/s, where Q_{mf} is the volumetric flow rate for minimum fluidization. The other operating conditions and material properties are the same as before. The Syamlal-O'Brien drag model was used for all side-gas simulations.

Figure 9 compares contour plots of the simulated time-averaged gas holdup within the fluidized bed operating at $U_g = 2U_{mf}$ with $Q_s = 0.2Q_{mf}$ with X-Z and Y-Z slice experimental data. It can be seen from Figure 9 that the side-gas injection causes obvious asymmetry throughout the entire fluidized bed. In Figure 9c, a region of relatively high gas holdup is observed directly above the injection port. The overall fluidized-bed dynamics are strongly influenced by side-gas injection. With side-gas injection, a path of high gas holdup extends from the injection port to the bed surface. This region of high gas holdup gradually expands into the bed as it rises, indicating that horizontal gas dispersion increases with axial height. However, the CFD simulations do not exactly predict the gas dispersion rate. As shown in Figure 9d, the extent of side-gas dispersion with height is under predicted. The side-gas injection does not break up the bulk circulation regions throughout the fluidized bed; rather its effect is limited to the region near the wall. Side-gas injection also produces a nonuniform average bed height above the injection port. The highest average bed height occurs near the wall, directly above the injection port.

Quantitative local gas holdup comparisons between simulations and experimental data at different horizontal levels are shown in Figure 10. The horizontal level $Z = 0.25D$ is just above the side-gas injection port, where the maximum gas holdup is above 0.9. In this region, the simulations capture the effect of side-gas injection and quantitatively agree with the experimental data. As seen in Figures 10b–d, the injected gas expands further into the bed along the axial height from one-quarter to one-half of the bed diameter, where the maximum gas holdup in the Y-Z slice decreases to about 0.72 and 0.68 for the experiments and simulations, respectively. In comparison, the X-Z slice gas holdup ranges between about 0.44–0.62 experimentally and 0.44–0.52 computationally throughout the rest of the fluidized bed because side-gas injection has little influence in regions away from the injection port, which remain somewhat symmetric.

Velocity field

Figure 11 compares the simulated time-averaged velocity field of the glass beads in the fluidized bed operating at $U_g = 2U_{mf}$ without and with side-gas injection at $Q_s = 0.2Q_{mf}$ on the Y-Z slice in a 3D simulation using the Syamlal-O'Brien drag model. It can be seen from Figure 11a that there are two large circulation zones in the fluidized bed and each occupies nearly half of the bed. When the air is injected from the side port, the circulation zone on the injection side is changed completely, as shown in Figure 11b. The velocity of the glass beads without side-gas injection (Figure 11a) move downwards along the walls, but move upward along the wall with side-gas injection. In contrast, with side-gas injection the circulation zone on the opposite side of the bed is hardly affected.

Conclusions

CFD simulations using the Euler-Euler model in Fluent 6.3 for a lab-scale bubbling fluidized bed containing Geldart Group B particles have been validated using experimental local time-averaged gas holdup data. Simulation results in 2D are used to determine the required grid resolution (4×4 mm^2) for grid-independent predictions of the local gas holdup data. 3D simulations using three different drag models with or without side-gas injection are then compared to experimental data. Results from this study are useful for understanding how the local time-averaged gas holdup varies in the fluidized bed, and how well the CFD model captures the experimentally observed gas holdup distribution. Furthermore, because it establishes the CFD model parameters needed to accurately capture the local gas holdup, the simulation results will be useful for the design of commercial-scale fluidized-bed reactors for biofuel processing.

The experimental procedure using X-ray CT is demonstrated to be a good noninvasive technique for obtaining detailed local time-averaged gas holdup information in an opaque fluidized-bed reactor. The experimental results show that the cross section of the fluidized bed contains two large symmetric regions in which the time-average gas holdup is larger than in the middle of the fluidized bed. This experimental observation is well predicted by the CFD model. Overall, the CFD simulations with the Syamlal-O'Brien and Gidaspow drag models yield good predictions for the gas holdup throughout the fluidized bed, compared with the experimental data. In comparison, the gas holdup in the CFD simulations with the Wen-Yu drag model is generally over predicted. With side-gas injection, the injected gas penetrates further into the fluidized bed in the experiments as compared

to the CFD predictions. Nevertheless, because the side-gas injection has little effect on the overall gas holdup, the CFD predictions away from the injection port are in good agreement with the experiments.

Acknowledgments

Support for this research was provided by the ConocoPhillips Company. The X-ray facility used in this research was funded by the National Science Foundation under award number CTS-0216367 and Iowa State University.

Notation

A = X-ray attenuation of the dynamic fluidized bed
A_g = X-ray attenuation of the gas
A_p = X-ray attenuation of the individual particle
Ar = Archimedes number
d_s = particle diameter, m
e_{ss} = coefficient of restitution for particle collisions
g = gravitational acceleration, m/s^2
$g_{0,ss}$ = radial distribution coefficient
I = intensity of the dynamic fluidized bed
I_b = intensity of a static (bulk) bed of particles
I_g = intensity of the gas
I_p = intensity of an individual particle
$\bar{\bar{I}}$ = stress tensor
I_{2D} = second invariant of the deviatoric stress tensor
K_{gs} = coefficient for the interphase force, kg/(m^3 s)
k_{θ_s} = diffusion coefficient for granular energy
P_g = pressure in gas phase, Pa
P_s = pressure in solid phase, Pa
Q_{mf} = gas flow rate, m^3/s
Q_s = side-gas flow rate, m^3/s
Re_s = Reynolds number for the solid phase
U_g = superficial gas velocity, m/s
U_{mf} = minimum fluidization velocity, m/s
v_g = velocity for the gas phase, m/s
$v_{r,s}$ = terminal velocity for the solid phase, m/s
v_s = velocity for the solid phase, m/s

Greek letters

ε_g = volume fraction of the gas phase
$\varepsilon_{g,b}$ = volume fraction of the bulk material
ε_s = volume fraction of the solid phase
$\varepsilon_{s,max}$ = maximum volume fraction of the solid phase
θ_s = granular temperature, m^2/s^2
λ_s = solids bulk viscosity, Pa s
μ_g = gas shear viscosity, Pa s
μ_s = solids shear viscosity, Pa s
$\mu_{s,fr}$ = frictional viscosity for solid phase, Pa s
$\mu_{s,kin}$ = kinetic viscosity for solid phase, Pa s
$\mu_{s,col}$ = collisional viscosity for solid phase, Pa s
ρ_g = density of the gas phase, kg/m^3
ρ_s = density of the solid phase, kg/m^3
$\bar{\bar{\tau}}_g$ = gas-phase stress tensor, Pa
$\bar{\bar{\tau}}_s$ = solid-phase stress tensor, Pa
γ_{θ_s} = collisional dissipation of energy, kg/(s^3 m)
ϕ = angle of internal friction, deg
Φ_{gs} = transfer rate of kinetic energy, kg/(s^3 m)

Literature Cited

1. Heindel TJ, Gray JN, Jensen TC. An X-ray system for visualizing fluid flows. *Flow Meas Instrum*. 2008;19:67–78.
2. Franka NP, Heindel TJ, Battaglia F. Visualizing cold-flow fluidized beds with X-rays. In: *Proceedings of IMECE2007: 2007 ASME International Mechanical Engineering Congress and Exposition*. Seattle, WA: ASME Press, 2007: Paper IMECE2007-43073.
3. Cui H, Grace JR. Fluidization of biomass particles: a review of experimental multiphase flow aspects. *Chem Eng Sci*. 2007;62:45–55.
4. Peirano E, Delloume V, Leckner B. Two- or three-dimensional simulations of turbulent gas–solid flows applied to fluidization. *Chem Eng Sci*. 2001;56:4787–4799.
5. Cammarate L, Lettieri P, Micale DMG, Colman D. 2D and 3D CFD simulations of bubbling fluidized beds using Eulerian-Eulerian models. *Int J Chem React Eng*. 2003;1:A48.
6. Darton RC, LaNauZe RD, Davidson JF, Harrison D. Bubble growth due to coalescence in fluidised beds. *Trans Am Inst Chem Eng*. 1977;55:274–280.
7. Xie N, Battaglia F, Pannala S. Effects of using two- versus three-dimensional computational modeling of fluidized beds. Part II. Budget analysis. *Powder Technol*. 2008;182:14–24.
8. Papadikis K, Bridgwater AV, Gu S. CFD modelling of the fast pyrolysis of biomass in fluidised bed reactors. Part A. Eulerian computation of momentum transport in bubbling fluidised beds. *Chem Eng Sci*. 2008;63:4218–4227.
9. Kunii D, Levenspiel O. *Fluidization Engineering*, 2nd ed. Boston: Butterworth-Heinemann, 1991.
10. Wen CY, Yu YH. Mechanics of fluidization. *Chem Eng Prog Symp Ser*. 1966;62:100–111.
11. Grace JR, Leckner B, Zhu J, Cheng Y. Fluidized beds. In: Crowe, CT, editor. *Multiphase Flow Handbook*. New York: Taylor & Francis, 2006:5.1–5.93.
12. Heindel TJ, Hubers JL, Jensen TC, Gray JN, Striegel AC. Using X-rays for multiphase flow visualization. In: *Proceedings of the 2005 ASME Fluids Engineering Division Summer Meeting and Exhibition*. Houston, TX: ASME Press, 2005: Paper FEDS2005–77359.
13. Gui N, Fan JR, Luo K. DEM-LES study of 3-D bubbling fluidized bed with immersed tubes. *Chem Eng Sci*. 2008;63:3654–3663.
14. Hoomans BPB, Kuipers JAM, Briels WJ, van Swaaij WPM. Discrete particle simulation of bubble and slug formation in a two-dimensional gas-fluidised bed: a hard-sphere approach. *Chem Eng Sci*. 1996;51:99–118.
15. Kafui KD, Thornton C, Adams MJ. Discrete particle-continuum fluid modelling of gas–solid fluidised beds. *Chem Eng Sci*. 2002;57:2395–2410.
16. Sinclair-Curtis JL, van Wachem B. Modeling particle-laden flows: a research outlook. *AIChE J*. 2004;50:2638–2645.
17. van Wachem BGM, Schouten JC, van den Bleek CM, Krishna R, Sinclair JL. Comparative analysis of CFD models of dense gas–solid systems. *AIChE J*. 2001;47:1035–1051.
18. Xu BH, Yu AB. Numerical simulation of the gas–solid flow in a fluidized bed by combining discrete particle method with computational fluid dynamics. *Chem Eng Sci*. 1997;52:2785–2809.
19. Cornelissen JT, Taghipour F, Escudié R, Ellis N, Grace JR. CFD modelling of a liquid-solid fluidized bed. *Chem Eng Sci*. 2007;62:6334–6348.
20. Enwald H, Peirano E, Almstedt AE. Eulerian two-phase flow theory applied to fluidization. *Int J Multiphase Flow*. 1996;22:21–66.
21. Gidaspow D. *Multiphase Flow and Fluidization*. Boston: Academic Press, 1994.
22. Lettieri P, Cammarata L, Micale GDM, Yates J. CFD simulations of gas fluidized beds using alternative Eulerian-Eulerian modelling approaches. *Int J Chem React Eng*. 2003;1:A5.
23. Simonin O. Prediction of the dispersed phase turbulence in particle-laden jets. In: *Gas–Solid flows*. New York: ASME Press, 1991:197–206.
24. van Wachem BGM, Almstedt AE. Methods for multiphase computational fluid dynamics. *Chem Eng J*. 2003;96:81–98.
25. Yu L, Lu J, Zhang X, Zhang S. Numerical simulation of the bubbling fluidized bed coal gasification by the kinetic theory of granular flow (KTGF). *Fuel*. 2007;86:722–734.
26. Lun CK, Savage SB, Jeffrey DJ, Chepurniy N. Kinetic theory for granular flow: inelastic particles in Couette flow and slightly inelastic particles in a general flowfield. *J Fluid Mech*. 1984;140:233–256.
27. Syamlal M. *The Particle-Particle Drag Term in a Multiparticle Model of Fluidization*, National Technical Information Service.

VA: Springfield, 1987, NTIS/DE87006500, DOE/MC/2353-2373.
28. Syamlal M, Rogers W, O'Brien TJ. *MFIX Documentation: Theory Guide*, Vol. 1. VA: National Technical Information Service, Springfield, 1993, DOE/METC-9411004, NTIS/DE9400087.
29. Schaeffer DG. Instability in the evolution equations describing incompressible granular flow. *J Differ Equations*. 1987; 66: 19–50.
30. Parmentier JF, Simonin O, Delsart O. A numerical study of fluidization behavior of Geldart B, A/B and A particles using an Eulerian multifluid modeling approach. In: Werther, J., et al. (Eds.). *Circulating Fluidized Bed Technology IX*, Hamburg, Germany, 2008.
31. Wang J, van der Hoef MA, Kuipers JAM. Why the two-fluid model fails to predict the bed expansion characteristics of Geldart A particles in gas-fluidized beds: a tentative answer. *Chem Eng Sci*. 2009;64:622–625.

Manuscript received Dec. 30, 2008, and revision received Aug. 15, 2009.